

Amorphous Exsolution of Fe₃O₄ Nanoparticles in SrTiO₃: A Path to High Activity and Stability in Photoelectrochemical Water-Splitting

Myeong-Jin Kim, Changhoon Lee, Yong-Ryun Jo, Wan-Gil Jung, Jun-Seok Ha, Ji Hoon Shim, Jae-Hoon Park, Sang-Wan Ryu, and Bong-Joong Kim*

Exsolution creates metal nanoparticles embedded within perovskite oxide matrices, promoting optimal exposure, even distribution, and robust interactions with the perovskite structure. Fe₃O₄, an oxidized form of Fe, is an attractive catalyst for photoelectrochemical (PEC) water-splitting due to its strong light absorption, excellent electrical conductivity, and chemical stability. However, exsolving Fe is challenging, often requiring harsh reduction conditions that can decompose the perovskite. Herein, hybrid composites are fabricated for PEC water-splitting by reductively annealing a solution of SrTiO₃ photoanode and Fe cocatalyst precursors. In situ transmission electron microscopy reveals uniform, high-density Fe particles exsolving from *amorphous* SrTiO₃ films, followed by film-crystallization at elevated temperatures. This innovative process extracts entire Fe dopants while maintaining structural stability, even at doping levels exceeding 50%. Upon air exposure, the embedded Fe particles oxidize to Fe₃O₄, forming a Schottky junction and enhancing light absorption. These conditions yield a high activity of 5.10 mA cm⁻² at 1.23 V versus reversible hydrogen electrode (an 11.86-fold improvement over SrTiO₃) from the 30% Fe-doped SrTiO₃, with excellent stability (97% retention) over 24 h. Theoretical calculations indicate that in the *amorphous* state, Fe–O bonds weaken while Ti–O bonds remain strong, promoting selective exsolution. The mechanisms driving *amorphous* exsolution versus crystal exsolution are elucidated.


1. Introduction

Photoelectrochemical (PEC) water-splitting, which generates carbon-free hydrogen with high energy storage capacity, has gained attention as part of efforts to address environmental pollution and reduce fossil fuel consumption, driving the development of advanced renewable energy systems.^[1–6] Despite its potential, PEC water-splitting faces significant obstacles including charge carrier recombination, high overpotential, and slow reaction kinetics, which impede its efficiency and stability. Among other strategies, hybrid composites, especially those coupling cocatalysts with metal–oxide supports, enhance PEC water-splitting efficiency and stability by effectively separating electron–hole pairs at the interface and quickly consuming remaining photoinduced carriers at the cocatalyst surface.^[7–13]

Exsolution has emerged as a sophisticated technique for promoting the surface segregation of metallic nanoparticles (NPs) on perovskite oxides under reducing conditions.^[14,15] This process typically involves incorporating reducible transition or noble metals into the B site of the perovskite structure before reduction.^[16–19] The resulting hybrid composites feature

M.-J. Kim, B.-J. Kim
School of Materials Science and Engineering
Gwangju Institute of Science and Technology (GIST)
123 Cheomdangwagi-ro, Buk-gu, Gwangju 61005, Korea
E-mail: kimbj@gist.ac.kr

C. Lee, J.-H. Park
Max Planck POSTECH Center for Complex Phase of Materials
Pohang University of Science and Technology
Pohang 37673, Korea

 The ORCID identification number(s) for the author(s) of this article can be found under <https://doi.org/10.1002/ssstr.202400450>.

© 2024 The Author(s). Small Structures published by Wiley-VCH GmbH. This is an open access article under the terms of the Creative Commons Attribution License, which permits use, distribution and reproduction in any medium, provided the original work is properly cited.

DOI: 10.1002/ssstr.202400450

C. Lee, J. H. Shim
Division of Advanced Materials Science
Pohang University of Science and Technology
Pohang 37673, Korea

Y.-R. Jo
GIST Advanced Institute of Instrumental Analysis (GAIA)
Electron Microscopy Laboratory
Gwangju Institute of Science and Technology
Gwangju 61005, Korea

W.-G. Jung
Korea Basic Science Institute
Gwangju 61186, Korea

J.-S. Ha
School of Chemical Engineering
Chonnam National University
Gwangju 61186, Korea

well-organized NPs embedded within the perovskite oxide matrix, leading to efficient exposure, uniform size and distribution, and robust adhesion/interaction between the metal NPs and the perovskite. This configuration offers substantial benefits for various energy and environmental applications.^[20–24]

Fe₃O₄ (magnetite), which can be easily formed by Fe oxidation, is an attractive cocatalytic material for PEC water-splitting due to several advantages: 1) strong light absorption, capturing most light in the UV–visible range;^[25] 2) excellent electrical conductivity (>100 S cm^{−1}) and rapid electron transfer between Fe²⁺ and Fe³⁺ within the crystals;^[26,27] 3) high chemical stability;^[28] and 4) the ability to form heterojunctions with perovskite oxides, thereby reducing charge recombination.^[29,30] However, the exsolution of Fe from perovskite oxides is challenging and typically requires high temperatures under severe reduction conditions such as low oxygen partial pressures, which can unfavorably lead to partial decomposition of the perovskite, such as the extraction of Sr, which is detrimental to PEC performance.^[31–33] For example, Fe is reported to be the most difficult to exsolve due to its low cosegregation energy among several transition metals doped in PrBaMn_{1.7}Ti_{0.3}O_{5–δ} (T = Mn, Co, Ni, and Fe).^[22]

Additionally, even for dopants such as Co, which are relatively easily exsolved from perovskite oxides like SrTiO₃, exsolution is constrained to enhance PEC reactivity and stability due to following reasons: 1) only limited portion of the dopants in the perovskite is exsolved because the exsolution occurs only within a narrow range (≈5 nm) from the oxide surface; and 2) increasing doping concentrations to achieve more exsolution degrades structural stability of the perovskite by increasing oxygen vacancies, thereby hampering PEC stability.^[34–36]

To address the aforementioned challenges, we introduce the “amorphous exsolution” technique, which involves annealing a spin-coated sol–gel solution containing the precursors of SrTiO₃ photoanode and Fe cocatalyst under mildly reducing environment (i.e., low hydrogen flow rates) to create a hybrid composite for PEC water-splitting. In situ TEM is employed to monitor the phase evolution of the oxide film and the growth properties of the cocatalysts at elevated temperatures (500–850 °C) under an oxygen partial pressure (*P*_{oxy}) of 10^{−17} Torr. All Fe dopants are exsolved from the amorphous oxide films at intermediate temperature ranges (500–800 °C for Fe doping below 50%), forming high-density NPs with uniform sizes and distributions, followed by complete crystallization of the oxide film at temperatures above this range. Upon exposure to air, the Fe particles are oxidized to Fe₃O₄ particles, which are partially embedded within the SrTiO₃ film, forming Schottky junctions at the interfaces for

efficient charge separation with enhanced light absorption. By combining quantitative particle analyses with PEC data, we find that the 30% Fe-doped photoanode exhibits the highest PEC activity and stability compared to other doping concentrations, due to the largest particle coverage on the film surface and smaller particle sizes. Through theoretical calculations and exsolution experiments on 30% Fe-doped SrTiO₃, fabricated by amorphous and crystal exsolution techniques under various gas environments (including air, vacuum, and various oxygen partial pressures), we elucidate the mechanisms underlying the complete process of amorphous exsolution and compare it to the crystal exsolution of the identical system. Table S1, Supporting Information presents various previous studies on SrTiO₃-based photoanodes, SrTiO₃-related photoanodes with NPs formed via crystal exsolution, and photoanodes featuring Fe₃O₄ cocatalysts, to emphasize the performance advantages (i.e., superior current density) of our work, called “amorphous exsolution”.

2. Results and Discussion

2.1. In Situ Observations of Fe Exsolution from SrTi_{1–x}Fe_xO₃ Films

To meticulously observe the formation and crystallization of Fe particles as well as the evolution of the underlying thin oxide layers, in situ transmission electron microscopy (TEM) was employed during the annealing process of SrTi_{1–x}Fe_xO₃ films (where *x* ranges from 0.1 to 0.7), synthesized via sol–gel spin-coating under a H₂ gas flow (*P*_{oxy} = 10^{−17} Torr). Figure 1g–l presents a sequence of TEM bright-field (BF) images capturing distinct regions of the sample with a 30% Fe concentration (SrTi_{0.7}Fe_{0.3}O₃). These images were extracted from a video recording the sample undergoing staged heating at temperatures of 500, 600, 700, 750, 800, and 850 °C, sequentially. Accompanying each image, the respective selected area electron diffraction (SAED) pattern is displayed to understand phase evolution and transformation (see the expanded views in Figure S1, Supporting Information). At 600 °C, we observe a number of Fe particles, with diameters ranging from 3.5 to 6.0 nm (Figure S2b, Supporting Information), exsolved from the SrTiO₃ film. The SAED pattern of the image reveals that the particles are crystalline Fe, as identified by the presence of weakly diffracted spots (evidenced by the green arcs in the SAED pattern of Figure 1h and JCPDS 87-0722) while the film is amorphous, as demonstrated by the diffused rings of SrTiO₃ film. The size of Fe particles increases with temperature, approaching saturation at a range of 6.5 to 10.5 nm when the temperature exceeds 750 °C (Figure S2b and S3b, Supporting Information). The film remains amorphous up to 750 °C and crystallizes at 800 °C (see the relevant SAED patterns, JCPDS 79-0176). Schematics in Figure 1aa describe these stages of Fe exsolution from an amorphous SrTiO₃ film, followed by the subsequent crystallization of the oxide film. Significantly, this trend continues across various Fe compositions, with the notable exception that the temperature required for film crystallization increases as the Fe composition rises (Figure 1). Specifically, the film with 70% Fe is not crystallized below 850 °C. We observe that the diffracted spots from the

J. H. Shim
Department of Chemistry
Pohang University of Science and Technology (POSTECH)
Pohang 790-784, Korea

J.-H. Park
Department of Physics
Pohang University of Science and Technology
Pohang 37673, Korea

S.-W. Ryu
Department of Physics
Chonnam National University
Gwangju 61186, Korea

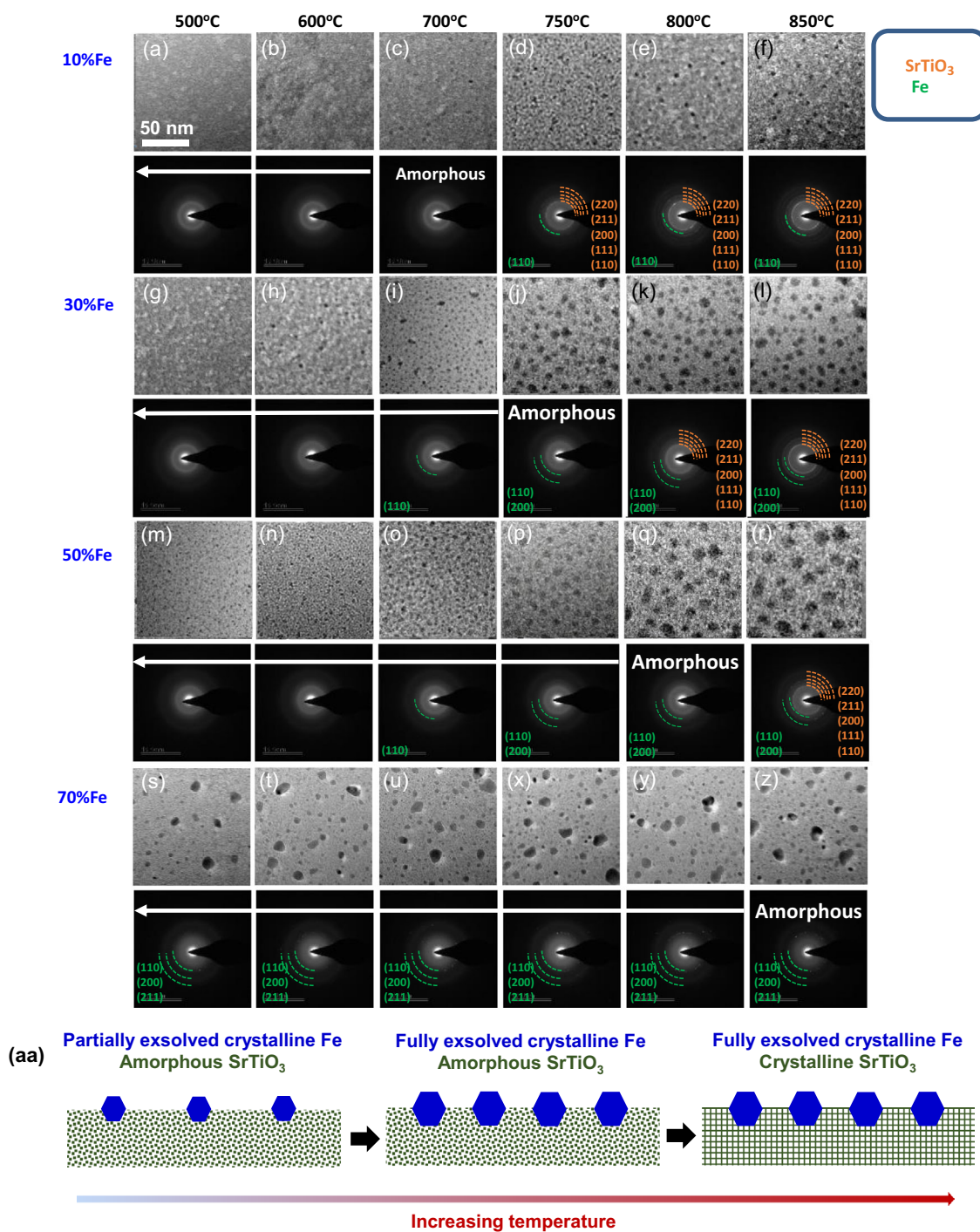


Figure 1. Real-time observations of the exsolution of Fe particles from $\text{SrTi}_{1-x}\text{Co}_x\text{O}_3$ films ($x = 0.1-0.7$) during reductive annealing at elevated temperatures. a–f) A series of TEM BF images of representative areas of the sample doped with 10% Fe, heated in stages to 500, 600, 700, 750, 800, and 850 °C, with the corresponding SAED pattern for each image. g–l) 30% Fe-doped sample. m–r) 50% Fe-doped sample. s–z) 70% Fe-doped sample. aa) Schematics depicting all stages of amorphous exsolution in Figure 1a–z.

Fe particles are not detected below 700 °C in the 10% Fe sample, 600 °C in the 30% Fe sample, and 600 °C in the 50% Fe sample, attributable to the minimal quantity of exsolved Fe atoms.

To confirm the presence of Fe crystals on amorphous films, high-resolution transmission electron microscopy (HRTEM) was

employed during annealing at 750 °C for the sample with 30% Fe doping. **Figure 2f** presents the HRTEM image of a single Fe crystal, alongside its corresponding fast Fourier transform (FFT) pattern, as shown in **Figure 2g**. The crystal structure of the particle is identified as BCC, which is the preferred structure below

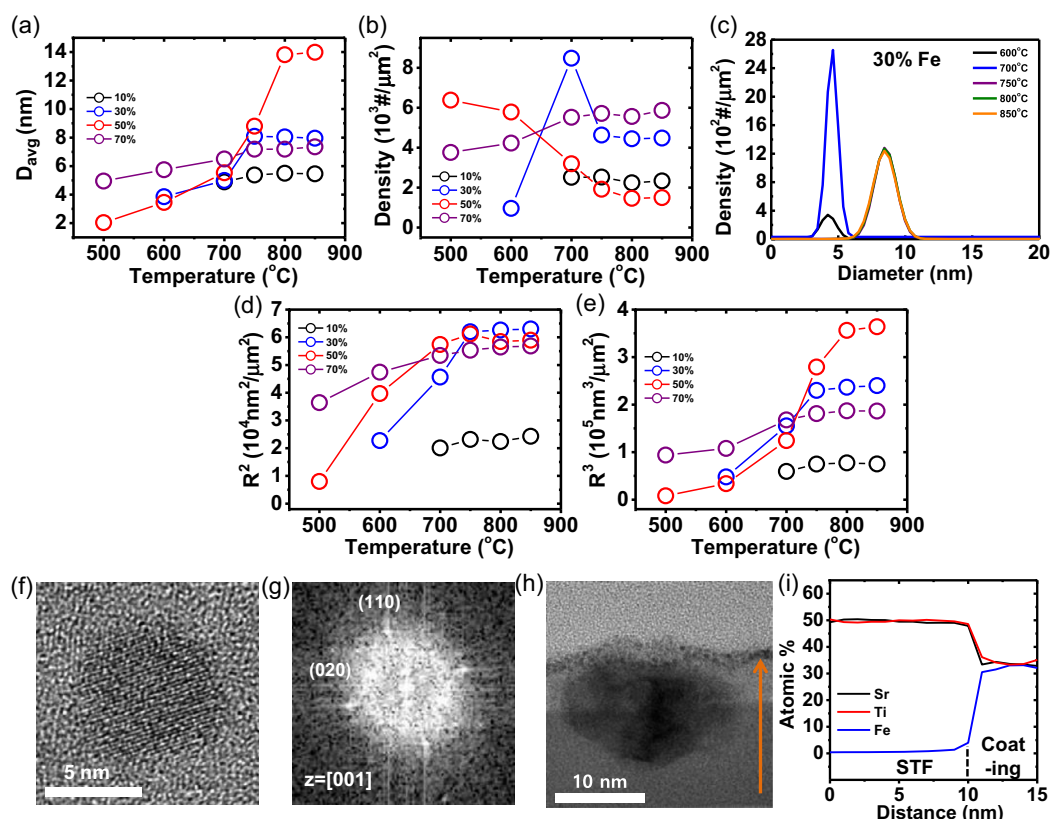


Figure 2. Quantitative analyses of exsolved Fe particles during reductive annealing and TEM analyses. a,b) Dependence of temperature on the average diameter and density of the particles, respectively, at all Fe concentrations. c) Size distributions of the particles at 30% Fe. d,e) Temperature dependence of the total surface area (R^2) and volume (R^3) of the particles at various Fe concentrations, respectively. f,g) An in situ HRTEM image of a single Fe particle generated from a 30% Fe sample while annealing at 750 °C, and the corresponding FFT pattern of the image, respectively. h,i) A cross-view TEM BF image of a Fe_3O_4 particle embedded into the SrTiO_3 film doped with 30% Fe and an EDX line scan profile following the arrow in Figure 2h.

911 °C,^[37] and the lattice spacings of (110) and (020) are 0.201 and 0.174 nm, respectively, in agreement with those of pure Fe crystal (JCPDS 87-0722). In contrast, the supported oxide film exhibits an amorphous nature without lattices.

2.2. Quantitative Analyses of Exsolved Fe Particles during Reductive Annealing

Real-time observations enable us to quantify the size evolution and density distribution of Fe particles at different temperatures through direct measurements of individual particles. We observe that the sizes of Fe particles rapidly reach saturation within tens of seconds and remain constant over an extended period (≈ 10 min), without further nucleation or coarsening after reaching to designated temperatures. Figure 2a,b shows how temperature affects the average diameter and density of the particles, respectively, across all Fe concentrations. It is evident that as temperature increases, the sizes and densities of the particles either increase or remain nearly constant until reaching saturation, beyond which the SrTiO_3 films crystallize because Fe exsolution occurs under suppressed particle coarsening. The only exception is the sample with 50% Fe doping, where the particle density decreases with temperature, opposite to the trend of average

diameter, due to severe particle coarsening during exsolution caused by the high doping concentration and high atomic diffusivity^[38] in the amorphous substrate. However, particle coarsening ceases after the crystallization of the film because diffusivity becomes lower in the crystalline state.^[38] In the case of 70% doping, despite the higher doping level, both particle size and density increase simultaneously. This is because a substantial amount of Fe has already exsolved at around 500 °C, resulting in significant coarsening at lower temperatures (see Figure 1s–z) and minimal increases in area and volume with temperature compared to the 30% Fe and 50% Fe samples (see Figure 2d,e). As a result, the spacing between particles becomes considerably larger, and with further temperature increases, almost no additional coarsening occurs. Thus, exsolved atoms either attach to existing particles, further increasing their size, or form new particles on the broad substrate areas between the existing particles.

Consequently, the total surface area (R^2) and volume (R^3) of the particles, plotted against temperature at various Fe concentrations, exhibit a consistent general trend as observed in Figure 2a,b (Figure 2d,e), suggesting Fe atoms continue to exsolve with increasing temperature and no further Fe atoms exsolve after reaching saturation. This behavior is corroborated by the particle size distributions, which show collapsed Gaussian plots across the temperature range (Figure 2c and S3, Supporting

Information). The thermal stability observed after the crystallization of the film, characterized by negligible aggregation or coarsening of particles, is attributed to the Fe particles embedded in the SrTiO_3 films, as demonstrated in Figure 2h.

Specifically, after exposure to air, the Fe particle is oxidized to the Fe_3O_4 particle while remaining embedded in the SrTiO_3 film. The particle has a FCC crystal structure, with lattice spacings of 2.96 nm for the (220) plane and 2.53 nm for the (311) plane (JCPDS 88-0866) (see the HRTEM image and FFT pattern in Figure S4, Supporting Information). The Fe composition remains nearly constant throughout the film, staying below 0.5% (less than 2.5% of the B site's composition), as exhibited in Figure 2h,i. This indicates nearly all Fe atoms are exsolved from the amorphous film during reductive annealing because the amount of extracted Fe atoms is saturated before the crystallization of the SrTiO_3 film (Figure 2). This trend continues beyond 50% Fe, which is referred to as "amorphous exsolution". This amorphous exsolution contrasts sharply with conventional exsolution from crystalline oxides, termed "crystal exsolution". In the 30% Fe-doped crystalline SrTiO_3 film, the Fe composition remains constant at 5.5% starting from ≈ 5 nm below the film surface, with only 0.5% of Fe atoms in total composition (2.5% of B site's composition) being exsolved, even under a lower oxygen partial pressure ($P_{\text{O}_2} = 10^{-19}$ Torr) than that used for

amorphous exsolution (see the cross-sectional TEM image and energy dispersive X-ray spectrometer (EDX) line scan in Figure S5, Supporting Information and the plan view TEM image in Figure 6p). Significant exsolution occurs only near the film surface. Such insufficient exsolution typically occurs in various oxide systems during crystal exsolution.^[34–36] Additionally, we note that the saturated R^2 of the particles in the samples with 30% and 50% Fe doping are similar due to the increased averaged particle sizes with higher Fe concentration.

2.3. X-ray Diffraction (XRD) and X-ray photoelectron Spectroscopy (XPS) Analyses of $\text{SrTi}_{1-x}\text{Fe}_x\text{O}_3$ Films after Exsolution

To corroborate the crystal structures of the phases observed during the in situ TEM work, XRD spectroscopy was performed. The XRD data acquired from the samples with various Fe doping concentrations after annealing at 850 °C under $P_{\text{O}_2} = 10^{-17}$ Torr are shown in Figure 3a. The spectra from the samples with 0%–50% Fe doping exhibit strong SrTiO_3 peaks (JCPDS 79-0176). Above 70% Fe, the SrTiO_3 peaks are completely absent because the SrTiO_3 is amorphous. The (220) and (311) peaks of Fe_3O_4 appear at 30%–70% Fe doping (JCPDS 88-0866), indicating the oxidation of Fe particles, except at 10%, where

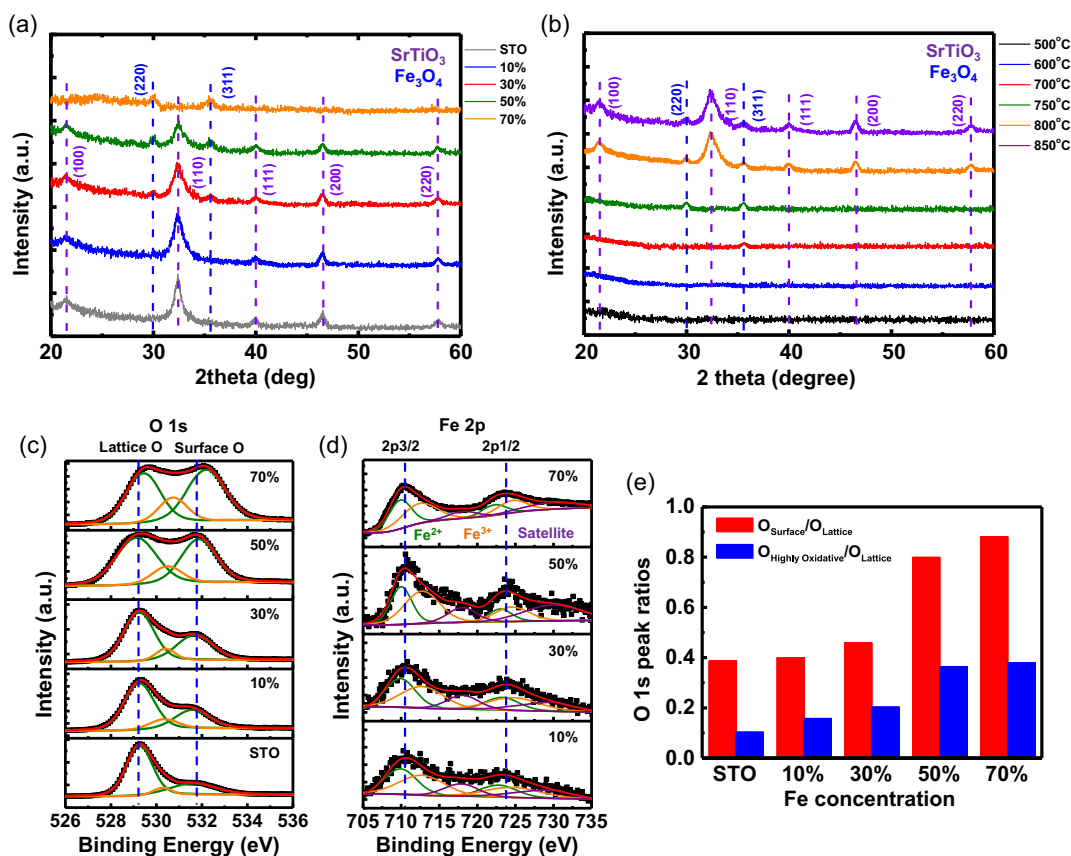


Figure 3. XRD and XPS analyses of the $\text{SrTi}_{1-x}\text{Fe}_x\text{O}_3$ films ($x = 0.1$ – 0.7) after and during reductive annealing. a) Data acquired from the samples with all the Fe doping concentrations after annealing at 850 °C under a H_2 gas flow. b) Data acquired from the sample doped with 30% Fe after annealing at various temperatures under a H_2 gas flow. c,d) O 1s and Fe 2p spectra of the samples with various Fe concentrations. e) The ratios of surface O/lattice O and highly oxidative O/lattice O at various Fe concentrations.

the amount of exsolved Fe is too small to be detected. The XRD spectra obtained from the 30% Fe samples annealed at various temperatures and under $P_{\text{oxy}} = 10^{-17}$ Torr are exhibited in Figure 3b, confirming the crystallization process of the Fe particles and the SrTiO₃ film, as observed using in situ TEM in Figure 1.

To investigate the relationship between the oxygen chemical environment and different Fe doping levels, XPS analysis was conducted on the same samples, as shown in Figure 3a. The O 1s spectra for samples with varying Fe concentrations are presented in Figure 3c. The spectra primarily exhibit three peaks corresponding to different oxygen species in SrTiO₃: lattice oxygen (O^{2-}) at 529.2 eV, highly oxidative oxygen (O^- , O_2^{2-}) at 530.3 eV, and surface oxygen ($-\text{OH}$) at 531.8 eV.^[36,39,40] The lattice O peak retains the same binding energy up to 50% Fe but it shifts to a higher binding energy of 529.6 eV at 70% Fe, likely due to the formation of amorphous SrTiO₃ (a similar trend is observed in the Sr 3d spectra shown in Figure S6a, Supporting Information).^[41] Furthermore, up to 50% Fe, the surface oxygen and the highly oxidative oxygen peaks retain the similar binding energies, while their intensities increase relative to the lattice oxygen peaks as temperature increases (see the ratios in Figure 3e). This suggests the generation of more oxygen vacancies during Fe exsolution at higher Fe concentrations, which promotes the formation of other oxygen-containing species, such as the $-\text{OH}$ group, on the film surface.^[36] The Fe 2p spectrum can be deconvoluted into six peaks with two main peaks of Fe 2p_{3/2} and Fe 2p_{1/2} at 710.2 and 723.7 eV, as shown in Figure 3d. The two peaks (in green) located at 710 and 722.5 eV can be attributed to 2p_{3/2} and 2p_{1/2} of Fe²⁺ species.^[42,43] And the other two peaks (in orange) at binding energies of 712.5 and 725 eV correspond to 2p_{3/2} and 2p_{1/2} of Fe³⁺ species.^[41,44] The remaining two peaks (in purple) at 717.7 and 729.7 eV are satellite peaks, indicating the formation of Fe₃O₄ particles on the film surface.^[45]

2.4. PEC Water-Splitting Performances of SrTi_{1-x}Fe_xO₃ Samples after Exsolution

We further investigated the effect of Fe doping on the PEC water-splitting performance of the SrTi_{1-x}Fe_xO₃ samples used as photoanodes, following thermal reduction at 850 °C under $P_{\text{oxy}} = 10^{-17}$ Torr. Linear sweep voltammetry (LSV) curves reveal a significant increase in photocurrent densities for all photoanodes under illumination compared to dark conditions. This increase ranges from 18.75% to 251.72% at 1.23 V versus reversible hydrogen electrode (RHE), depending on the Fe concentration (Figure 4a and Table S2, Supporting Information). The photocurrent density at 1.23 V versus RHE initially rises with increasing Fe concentration, peaking at 5.10 mA cm⁻² for 30% Fe, which is an 11.86-fold improvement over bare SrTiO₃. This improvement is attributed to the electric field in the space-charge region at the interface between the SrTiO₃ photoanode and Fe₃O₄ cocatalysts, as described in Figure 4e,f, which facilitates the separation of photogenerated charges.^[46] The current density achieved in our work is superior to those reported in previous studies (see Table S1, Supporting Information). We will discuss the detailed estimation of the band diagrams of the

materials before and after they join each other, and the effects of the junction in the next section.

However, beyond 30% Fe, the photocurrent density dramatically decreases by 52% to 2.46 mA cm⁻² at 50% Fe due to increased Fe₃O₄ particle sizes and the similar surface coverage of the particles as at 30% Fe (Figure 2a,d). This results in longer specific diffusion lengths for the photo-holes, and reduced light absorption.^[47,48] The photocurrent density continues to decrease by 96% to 0.19 mA cm⁻² at 70% Fe due to the formation of an amorphous SrTiO₃ film (see Figure 1z), which can form numerous defects that act as trap recombination centers within its forbidden band.^[49,50] Electrochemical impedance spectroscopy (EIS) supports the LSV results, showing that the diameter of the semicircle decreases up to 30% Fe, and then increases (Figure 4b).^[51,52]

Figure 4c displays the applied-bias photon-to-current conversion efficiency (ABPE) (see details in Supporting Information). Initially, ABPE increases with Fe concentration: 0.47% at 0.45 V for 10% Fe and 1.54% at 0.62 V for 30% Fe, representing over a 2.61-fold and 8.56-fold improvement compared to bare SrTiO₃, respectively. However, at higher Fe concentrations, photoconversion efficiency significantly decreases to 1.00% at 0.42 V for 50% Fe and falls below that of bare SrTiO₃ at 70% Fe. Long-term stability tests of the photoanodes were conducted at 1.23 V versus RHE under illumination for 24 h, as shown in Figure 4d. The photoanode with 30% Fe demonstrates the highest consistency with only a decline rate of $\approx 3\%$ per day and the highest current density. This is attributed to the largest surface coverage of Fe₃O₄ particles on the SrTiO₃ photoanode and smaller particle sizes compared to those at 50% Fe (Figure 2a,d). These particles enhance charge separation/transfer and passivate the surface states of the photoanode, thereby preventing photocorrosion by consuming the remaining photoinduced holes.^[39,40] For other Fe concentrations, photocurrent density and/or stability decrease considerably due to the reduced surface coverage of Fe₃O₄ particles and/or larger particle sizes (Figure 2a,d). We confirm that the SrTiO₃ film and Fe₃O₄ particles remain largely unchanged after the oxygen evolution reaction (OER) reaction. This is supported by the XRD and XPS spectra of the 30% Fe-doped SrTiO₃ sample obtained after the stability test (Figure S7 and S8, Supporting Information). The data show results that are nearly identical to those measured prior to the stability test. Additionally, the dissolved Fe from the 30% Fe-doped sample in the electrolyte after a 24-h stability test (see Figure 4d) was analyzed using inductively coupled plasma mass spectrometry. The concentration of dissolved Fe was estimated to be ≈ 0.48 nmol, which is about 2.8% of the total Fe content in the Fe₃O₄ particles embedded in the SrTiO₃ film, consistent with the stability test results. This small amount of dissolved Fe confirms the high stability of the optimized sample.

2.5. Estimating Electronic Band Structures and Understanding PEC Efficiencies

To estimate the band structures of the optimized photoanodes, the 30% Fe-doped SrTiO₃, and to understand the impact of the SrTiO₃/Fe₃O₄ heterostructures on PEC performance, we utilized a range of analytical techniques. These include UV-visible

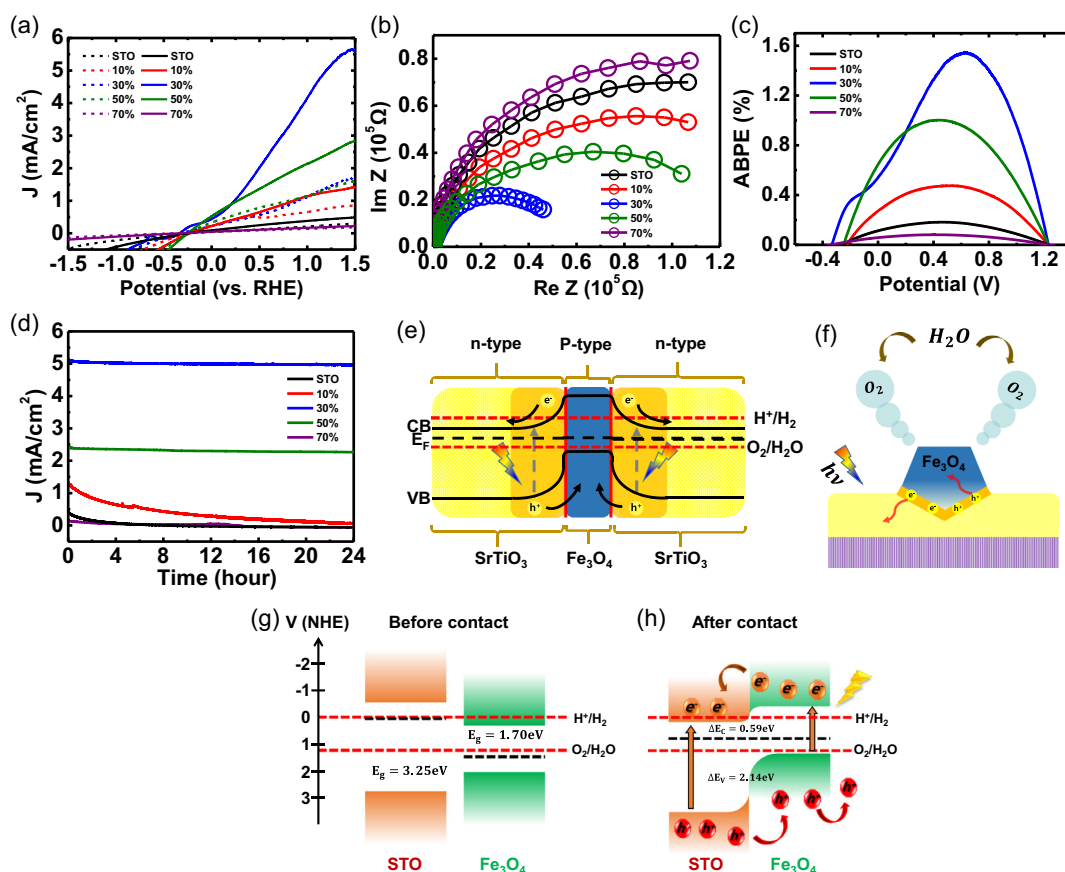


Figure 4. PEC water-splitting performance of the $\text{SrTi}_{1-x}\text{Fe}_x\text{O}_3$ samples ($x = 0.1\text{--}0.7$) as photoanodes after reductive annealing at 850°C . a–d) Influence of Fe doping on LSV, EIS, ABPE, and long-term stability, respectively. e, f) Schematics describing the charge separation in the space-charge region at the $\text{SrTiO}_3\text{--Fe}_3\text{O}_4$ interface and the oxygen evolution reaction. g, h) Band diagrams of a $\text{SrTiO}_3\text{--Fe}_3\text{O}_4$ photoanode before and after contact.

absorption spectroscopy (UV–vis), ultraviolet photoelectron spectroscopy (UPS), Mott–Schottky (M–S), photoluminescence (PL), time-resolved photoluminescence (TRPL), incident photon-to-electron conversion efficiency, charge separation/transfer efficiencies, electrochemically active surface area (ECSA), and Faradaic efficiency (FE) measurements (see details of the techniques in Supporting Information).

The UV–vis absorption spectra of SrTiO_3 , Fe_3O_4 , and 30% Fe-doped SrTiO_3 photoanodes are displayed in Figure 5a, to assess their absorption capabilities in the 300 to 800 nm range. The SrTiO_3 and Fe_3O_4 films show light absorption edges at ≈ 374 and 748 nm, respectively. This information facilitates the estimation of the photoanodes' bandgaps, calculated to be 3.24 eV for SrTiO_3 ^[53,54] and 1.75 eV for Fe_3O_4 ,^[55,56] by drawing a tangent to the curve in the T_{auc} plot ($(\alpha h\nu)^{1/2}$ versus photon energy, Figure 5b) (see Equation (S2), Supporting Information). Notably, anchoring Fe_3O_4 particles into the SrTiO_3 films enhances light absorption compared to pristine SrTiO_3 and extends the light absorption region to ≈ 550 nm (Figure 5a). These behaviors contribute to the improved PEC performance as demonstrated above.

The electronic structures of SrTiO_3 and Fe_3O_4 were investigated using UPS (Figure 5c). This analysis determines the work function and the valence band maximum (VBM) relative to the

Fermi level (E_{F}).^[57] The work functions are calculated to be -4.45 eV for SrTiO_3 and -5.90 eV for Fe_3O_4 . Using the bandgaps obtained from UV–vis measurements, the valence band positions are determined to be -7.15 eV for SrTiO_3 and -6.46 eV for Fe_3O_4 . Correspondingly, the conduction band positions are calculated to be -3.90 eV for SrTiO_3 and -4.76 eV for Fe_3O_4 . The data obtained from UV–vis and UPS measurements are depicted in Figure 4g, providing an estimation of the band structures of the SrTiO_3 and Fe_3O_4 photoanodes. The resulting band alignment confirms the formation of a type-II heterojunction between SrTiO_3 and Fe_3O_4 (Figure 4h), indicating a structure that facilitates efficient charge separation, beneficial for the oxygen evolution reaction.

M–S measurements were performed to gain qualitative insights into the formation of p–n junctions in the photoelectrodes (Figure 5d). The positive and negative slopes confirm that SrTiO_3 and Fe_3O_4 are n-type and p-type semiconductors, respectively.^[46,58] The flat band potentials (E_{fb}) of SrTiO_3 , Fe_3O_4 , and 30% Fe-doped SrTiO_3 were determined by extrapolating the x -intercepts from the M–S equation^[59] (see Equation (S3), Supporting Information). The flat band potentials obtained are -0.05 V for SrTiO_3 , 0.36 V (E_{fb}) and 1.23 V (E_{fb}) for 30% Fe-doped SrTiO_3 , and 1.52 V for Fe_3O_4 (V vs RHE), respectively. These values demonstrate that the E_{fb} of SrTiO_3 shifts

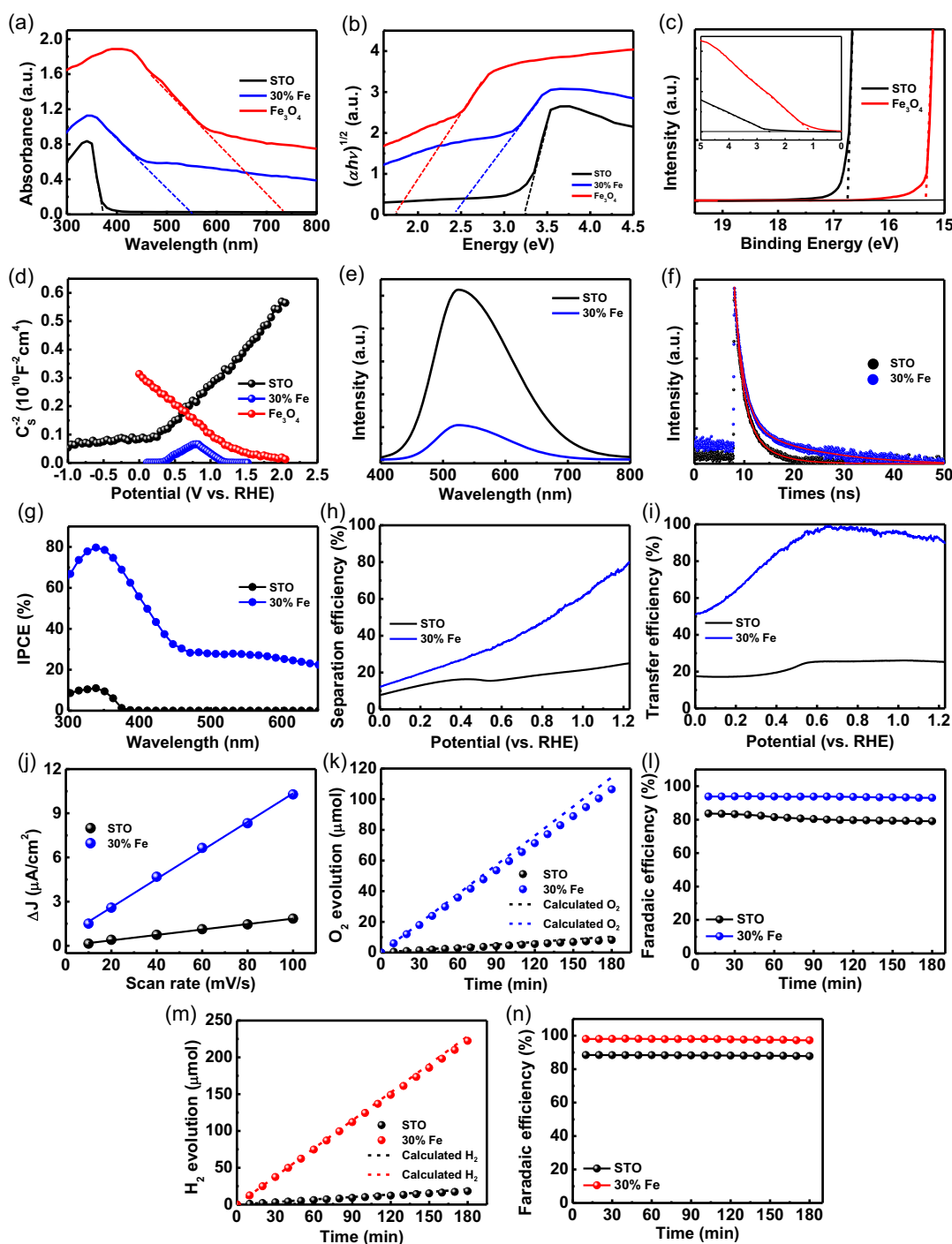


Figure 5. Characterization of electronic band structures, optical properties, and PEC efficiencies of $\text{SrTiO}_3\text{-Fe}_3\text{O}_4$ (fabricated from $\text{SrTi}_{0.7}\text{Fe}_{0.3}\text{O}_3$), SrTiO_3 , and Fe_3O_4 photoanodes. a,b) UV-vis adsorption spectra and their $Tauc$ plots, c) secondary cut-off region and valence band region of UPS spectra, d) M-S plots, e) PL spectra, f) TRPL spectra, g) IPCE plots, h) bulk charge separation efficiencies, i) surface charge transfer efficiencies, j) ΔJ versus scan rate plot, k) time-course O_2 evolution plots, l) time-course Faradaic efficiency plots, m) time-course H_2 evolution plots, and n) time-course Faradaic efficiency plots. Here, STO refers to SrTiO_3 .

positively and the E_{fb} of Fe_3O_4 shifts negatively after forming the type-II heterostructure between SrTiO_3 and Fe_3O_4 . These shifts indicate the Fermi levels of n-type SrTiO_3 shift downward, and those of p-type Fe_3O_4 shift upward, along with energy bands in

the heterostructure. Such behavior increases band bending, enhancing the separation of photogenerated charges and facilitating more photogenerated holes reaching the electrode surface (Figure 4g,h). Additionally, the carrier density (N_D) in the

photoanodes can be estimated from the slopes of the linear portions for the M-S plots^[60] (see Equation (S3), Supporting Information). The carrier densities are 2.64, 27.3, and $9.54(E_{\text{fb}})$ and $68.1(E_{\text{fb}}) \times 10^{18} \text{ cm}^{-3}$ for SrTiO₃, Fe₃O₄, and 30% Fe-doped SrTiO₃, respectively, implying that the Fe₃O₄ particles embedded in SrTiO₃ enhance charge transport properties, thus improving PEC performance.

PL emission spectra serve as an effective tool to understand of the recombination process of photogenerated electrons and holes. A higher intensity in the steady-state PL emission spectrum indicates faster recombination of photogenerated charges, which reduces photocatalytic activity.^[61,62] Figure 5e shows the steady-state PL spectra of SrTiO₃% and 30% Fe-doped SrTiO₃ photoanodes, with prominent peaks around 525 nm, mainly attributed to the oxygen vacancies near the SrTiO₃ surface.^[63] The PL intensity of 30% Fe-doped SrTiO₃ photoanodes is significantly lower than that of SrTiO₃, indicating that the SrTiO₃/Fe₃O₄ heterostructure effectively suppresses the recombination of photogenerated charge carriers. The TRPL curves of SrTiO₃% and 30% Fe-doped SrTiO₃ photoanodes were fitted by Equation (S4), Supporting Information (Figure 5f), and the average lifetimes (τ_{avg}) were calculated according to Equation (S5), Supporting Information. As listed in Table S3, Supporting Information, the average lifetime of the 30% Fe-doped SrTiO₃ photoanode (11.42 ns) is longer than that of the SrTiO₃ (3.43 ns), confirming that Fe₃O₄ particles embedded in the SrTiO₃ surface effectively reduce charge recombination within the film.

To assess the photoresponse of the photoanodes, IPCE measurements were performed in the 300–650 nm wavelength range at 1.23 V versus RHE. The 30% Fe-doped SrTiO₃ exhibits an IPCE value of 79.7% at 339 nm, significantly higher than the $\approx 10.9\%$ observed for pristine SrTiO₃ at the same wavelength (Figure 5g). The 30% Fe-doped SrTiO₃ photoanode shows excellent solar-to-current conversion efficiency across the 300–590 nm spectrum, consistent with the photocurrent density observed in the LSV curve. The onset wavelength of the photoanode is red-shifted compared to that of SrTiO₃, as verified by their T_{auc} plots (Figure S9, Supporting Information), indicating the establishment of a type-II band alignment.

To uncover the mechanisms behind the enhanced PEC performance, studies on bulk charge separation and surface charge transfer dynamics of SrTiO₃ and 30% Fe-doped SrTiO₃ photoanodes were conducted by comparing their LSV curves obtained under the water and sulfite oxidation conditions (Figure S10, Supporting Information). The efficiencies of bulk charge separation (η_{bulk}) and surface charge transfer (η_{surf}) were calculated to determine the effects of Fe₃O₄ cocatalysts, using Equation (S8) and (S9), Supporting Information, respectively. The 30% Fe-doped SrTiO₃ exhibits a η_{bulk} value of 80%, which is 3.2 times higher than the 25% observed for SrTiO₃ at 1.23 V versus RHE (Figure 5h). This increase is mainly attributed to the type II band alignment at the interface between the SrTiO₃ film and Fe₃O₄ particles, promoting effective charge separation. Additionally, the η_{surf} value for 30% Fe-doped SrTiO₃ reaches 90%, which is 3.6 times greater than the 25% for SrTiO₃ at 1.23 V versus RHE (Figure 5i). This superior η_{surf} for the 30% Fe-doped SrTiO₃ is due to Fe₃O₄ particles enhancing charge transfer

kinetics and minimizing surface recombination through surface passivation.

To evaluate the OER properties at the photoanode surface, the ECSA is typically measured. This is determined from the electrochemical double-layer capacitance (C_{dl}), which is directly proportional to the ECSA^[64] (see Equation (S11), Supporting Information). The C_{dl} s of the SrTiO₃ and 30% Fe-doped SrTiO₃ photoanodes were calculated from the slopes of their plots of Δj versus scan rates (Figure 5j), derived from the cyclic voltammetry curves (Figure S11, Supporting Information). The 30% Fe-doped SrTiO₃ achieves a C_{dl} of 0.484 mF cm^{-2} , significantly higher than the 0.092 mF cm^{-2} observed for SrTiO₃. This substantial increase in active sites at the surface is attributed to the Fe₃O₄ cocatalytic particles, which enhance the η_{surf} , as discussed in Figure 5i.

To ensure the photocurrent is effectively used for water oxidation, the Faradaic efficiency of the evolved O₂ and H₂ gases was measured. The gas evolution over time for SrTiO₃% and 30% Fe-doped SrTiO₃ photoanodes during a 3-h period is shown in Figure S12a,c, Supporting Information, respectively, with the corresponding Faradaic efficiencies in Figure S12b,d, Supporting Information. The results indicate stoichiometric production of H₂ and O₂, confirming successful water splitting. Figure 5k compares the actual O₂ evolution rates with theoretical predictions, showing that the 30% Fe-doped SrTiO₃ photoanode produces O₂ at a rate of $35.47 \mu\text{mol h}^{-1}$, which is about 13 times higher than the $2.72 \mu\text{mol h}^{-1}$ rate of SrTiO₃. Additionally, Figure 5l highlights that the Faradaic efficiency for the 30% Fe-doped SrTiO₃ reaches $\approx 93.1\%$, significantly surpassing the $\approx 79.0\%$ efficiency of SrTiO₃, indicating more effective utilization of photogenerated holes for oxygen evolution. Figure 5m presents a comparison between the actual H₂ evolution rates and the theoretical expectations, revealing that the 30% Fe-doped SrTiO₃ photoanode achieves a production rate of $74.72 \mu\text{mol h}^{-1}$, which is ≈ 12.3 times greater than the $6.06 \mu\text{mol h}^{-1}$ rate observed for SrTiO₃. Furthermore, Figure 5n demonstrates that the Faradaic efficiency of the 30% Fe-doped SrTiO₃ reaches around 97.3%, significantly exceeding the 87.8% efficiency of SrTiO₃. This indicates a more efficient utilization of photogenerated electrons for hydrogen evolution.

2.6. Density Functional Theory (DFT) Calculations of Amorphous and Crystalline SrTi_{1-x}Fe_xO₃

To explore the exsolution behavior in both amorphous and crystalline SrTi_{1-x}Fe_xO₃ phases ($x = 0-1.0$), we employed DFT to assess electronic structures, bonding features, and vacancy formation energies (V_{O} and V_{Fe}). First, the density of states (DOS) (Figure S13c-f, Supporting Information) was analyzed to examine bonding and antibonding characteristics in Ti–O and Fe–O interactions, using crystal orbital Hamilton population (COHP)^[65] (Figure 6c,d). COHP values that are positive indicate bonding states, while negative values represent antibonding states. In SrTiO₃, the occupied states in the valence band and the unoccupied states in the conduction band are generated by Ti–O bonding and antibonding interactions, respectively. In SrTi_{0.5}Fe_{0.5}O₃, Fe–O interactions in both amorphous and crystalline phases show antibonding characteristics near the

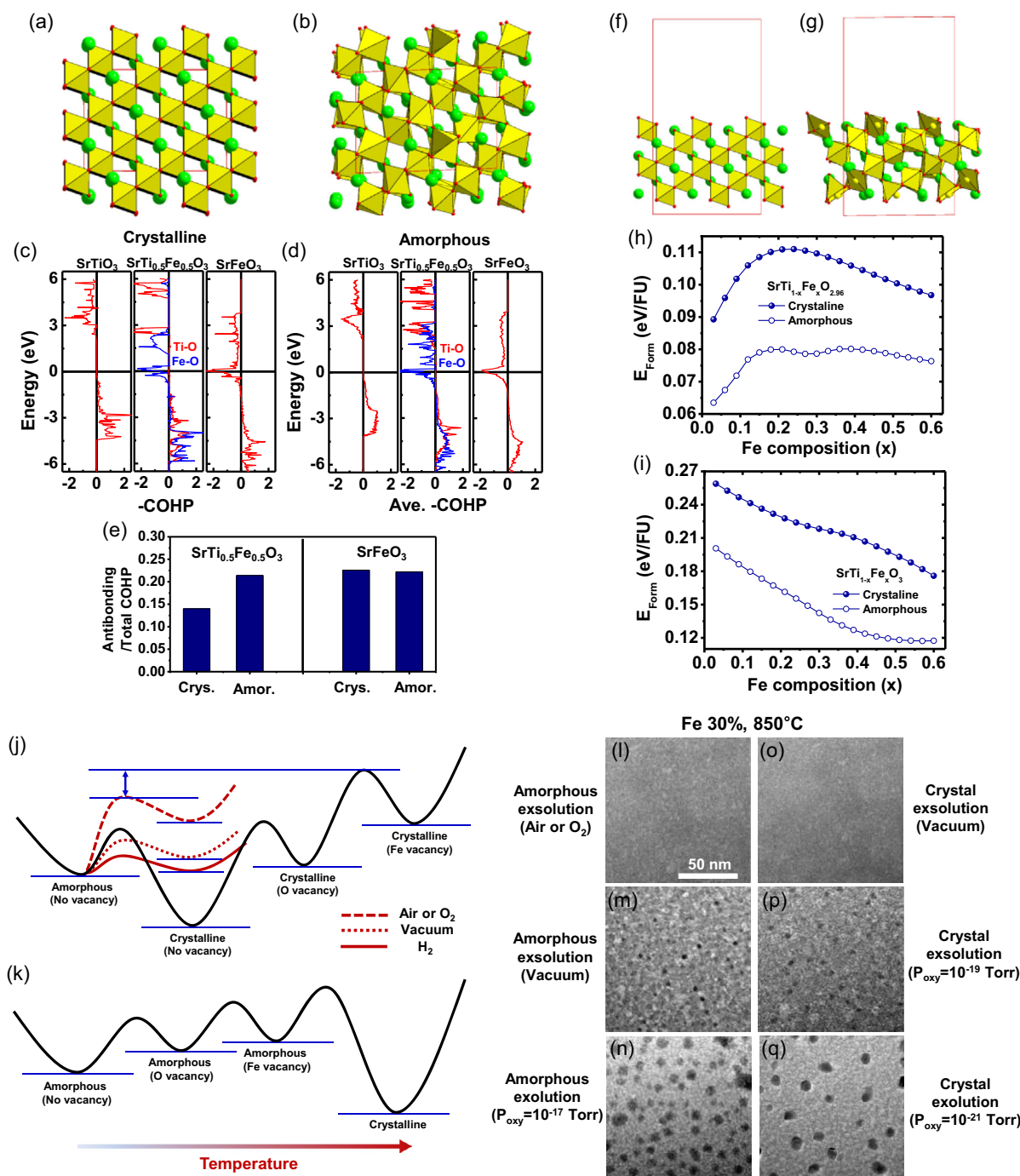


Figure 6. DFT calculations of the electronic structures, bonding characteristics, and vacancy formation energies of amorphous and crystalline $\text{SrTi}_{1-x}\text{Fe}_x\text{O}_3$ ($x=0-1.0$), and an illustration of the amorphous exsolution processes of the Fe-doped system compared to crystal exsolution. a,b) Perspective (001) views of crystalline and amorphous $\text{SrTi}_{1-x}\text{Fe}_x\text{O}_3$. The green circles and yellow polyhedra refer to the Sr atom and Ti/FeO_6 octahedra, respectively. c,d) COHP plots calculated for the Ti-O and Fe-O bonds of crystalline and amorphous $\text{SrTi}_{1-x}\text{Fe}_x\text{O}_3$ ($x=0, 0.5$, and 1), respectively. e) Antibonding/total COHP bar data for $\text{SrTi}_{0.5}\text{Fe}_{0.5}\text{O}_3$ and SrFeO_3 . f,g) Perspective (111) surface views of crystalline and amorphous $\text{SrTi}_{1-x}\text{Fe}_x\text{O}_3$ with a vacuum thickness of 14 Å. The color coding is the same as in Figure 6a,b. h,i) O and Fe vacancy formation energies plotted against Fe composition, respectively. The solid and hollow data represent the crystalline and amorphous phases, respectively. j) Energy landscape illustrating the criterion for determining crystal and amorphous exsolution. The red solid and short-dotted curves represent amorphous exsolution whereas the long-dotted curves represent crystal exsolution. The red long dotted, short dotted, and solid curves describe amorphous exsolution under air/ O_2 , vacuum, and H_2 gas flow, respectively. The black curve depicts the entire mechanism of crystal exsolution. k) Energy landscape illustrating the entire mechanism of amorphous exsolution. l-n) In situ TEM BF images of 30% Fe-doped samples annealed at 850 °C in air/ O_2 , vacuum, and H_2 atmospheres. o-q) In situ TEM BF images of 30% Fe-doped samples annealed under different reducing conditions (i.e., vacuum, $P_{\text{oxy}}=10^{-19}$ Torr, and $P_{\text{oxy}}=10^{-21}$ Torr).

VBM (≈ -1.0 to 0.0 eV), indicating weaker bond strengths compared to those in SrTiO_3 . Notably, in the amorphous phase, Fe—O antibonding interactions are more pronounced than in the crystalline phase, indicating a reduction in Fe—O bond strength (see integrated COHP in Figure 6e). Although both SrFeO_3 phases are metallic, the crystalline phase significantly intensifies antibonding interactions.

Subsequently, O and Fe vacancy formation energies were determined (Figure 6h,i) at the (111) surfaces (Figure 6f,g). The trends in vacancy formation energies for O and Fe are generally consistent: 1) vacancy formation energies in the amorphous phase are notably lower compared to the crystalline phase, a consequence of the diminished Fe—O bond strength discussed earlier; and 2) As Fe concentration increases, Fe vacancy formation energy decreases in both phases, attributed to the coordinate covalent bonding between Fe and O,^[66,67] which weakens the bond strength in comparison to the covalent bonding between Ti and O.^[68–71] The weakening of the bonds promotes exsolution in both phases and causes instability in the SrTiO_3 structure during the crystal exsolution.^[36] Interestingly, the initial increase in O vacancy formation energy at around 20% Fe composition is linked to the delocalization of electronic structures in Fe and Ti.

2.7. Thermodynamic Mechanism of Amorphous Exsolution in $\text{SrTi}_{1-x}\text{Fe}_x\text{O}_3$ in Comparison with Crystal Exsolution

Our concept of “amorphous exsolution” occurs when the energy required to form Fe vacancies is lower than the energy needed for crystallization from the amorphous state of the oxide support (illustrated by the red solid and short-dotted curves in Figure 6j). The entire mechanism is detailed in Figure 6k. In contrast, exsolution systems previously reported and fabricated through solution processes typically follow a “crystal exsolution” pathway, which occurs under conditions opposite to those required for amorphous exsolution (represented by the red long-dotted curve in Figure 6j). This mechanism adheres to the black landscape in Figure 6j.^[72–79] Notably, if the dopant cannot exsolve from the amorphous oxide, it must overcome a substantially higher energy barrier to form a vacancy within the crystal structure (indicated by the two-way arrow in Figure 6j).

Crystal exsolution systems are typically crystallized by calcining solutions in oxidizing conditions (air or oxygen environments) with low doping levels (less than 10% in B sites of perovskite), which inhibits oxygen vacancy formation and limits dopant exsolution.^[68] To investigate further, we annealed a 30% Fe-doped SrTiO_3 solution in different environments at 850°C . In air or under O_2 gas flow, no exsolution was observed due to the high Fe vacancy formation energy barrier imposed by these oxidative conditions (Figure 6l and the long-dotted red curve in Figure 6j). In contrast, under vacuum conditions, a few Fe particles were exsolved on the SrTiO_3 films, attributed to a lower Fe vacancy formation energy barrier (Figure 6m and the short-dotted red curve in Figure 6j). Notably, under a H_2 gas flow ($P_{\text{O}_2} = 10^{-17}$ Torr), the same condition in Figure 1, a significant amount of Fe particles (representing all Fe dopants) were exsolved on the film, due to the substantially reduced Fe vacancy formation energy barrier (Figure 3n and the solid red curve in Figure 3j).

To compare these conditions with crystal exsolution, we annealed the sample in Figure 6l under different degrees of reducing conditions. In vacuum, no exsolution occurs (Figure 6o), and under a oxygen partial pressure ($P_{\text{O}_2} = 10^{-19}$ Torr) (lower than that in Figure 6n), only a small amount of Fe is exsolved (Figure 6p and S5, Supporting Information). These behaviors are expected due to the high free energy barrier to form Fe vacancies compared to the driving forces provided by the two reducing conditions. When a lower oxygen partial pressure ($P_{\text{O}_2} = 10^{-21}$ Torr) is imposed, the film decomposes, exsolving both Sr and Fe, thereby forming SrO and Fe_3O_4 particles on the film after exposure to air (Figure S14a, Supporting Information), resulting in severely degraded PEC activity and stability (Figure S15, Supporting Information). Such poor PEC performance is ascribed to: 1) the large bandgap of SrO (5.7 eV) (Figure S16, Supporting Information), which causes reduced light absorption; 2) the large particles, which results in longer specific diffusion lengths for the photo-holes and reduced light absorption; and 3) a large amount of oxygen vacancies (Figure S14b, Supporting Information).^[47,48] Detailed explanations on the PEC performance of the crystal exsolution and relevant analyses are provided in Section 5, Supporting Information. Importantly, the total volume (R^3) of the SrO and Fe_3O_4 particles only reaches $\approx 71\%$ of that in amorphous exsolution (Figure 2e and 6n), implying that significantly fewer Fe dopants can be exsolved by crystal exsolution without decomposing Sr, regardless of the reducing conditions applied, such as low oxygen partial pressures.

3. Conclusion

Our amorphous exsolution technique extracts entire Fe dopants (over 50% doping concentrations) from amorphous SrTiO_3 films, forming high-density NPs uniformly embedded in the film surface. Subsequent annealing at higher temperatures crystallizes the film and eliminates oxygen vacancies formed during exsolution. Therefore, amorphous exsolution is highly effective for perovskite systems (ABO_3) where the B-site dopant-O bond strength is exceptionally high, allowing for the selective exsolution of dopants without decomposing the perovskite, while also ensuring structural stability. Such capabilities of our method enable us to achieve a high activity of 5.10 mA cm^{-2} at 1.23 V versus RHE (an 11.86-fold improvement over bare SrTiO_3) from the 30% Fe-doped SrTiO_3 photoanode, with highly consistent stability (97% retention) over 24 h. We believe that this innovative technique has the potential to significantly improve the performance of various heterogeneous catalyst systems in a wide range of energy and environmental applications. Additionally, the combination of in situ TEM and theoretical calculations has proven to be an exceptionally effective method for understanding the key parameters that determine the PEC activity and stability of hybrid composite photoelectrodes.

Supporting Information

Supporting Information is available from the Wiley Online Library or from the author.

Acknowledgements

M.-J.K. and C.L. have contributed equally to this work. This work is supported by the project numbers 2021R1A2C1005741, 2022M3C1A3091988, and RS-2024-00450652 funded by the National Research Foundation of Korea, the project number 2022M3H4A1A04074153 funded by the Ministry of Science and ICT, and GIST-MIT Research Collaboration. Portions of this work were conducted in Korea Basic Science Institute and GAIA in GIST.

Conflict of Interest

The authors declare no conflict of interest.

Author Contributions

Myeong-jin Kim: Data curation (lead); Formal analysis (lead); Investigation (lead); Visualization (lead); Writing—original draft (lead). **Changhoon Lee:** Data curation (lead); Formal analysis (lead); Investigation (lead); Writing—original draft (lead). **Yong-Ryun Jo:** Data curation (lead); Formal analysis (lead); Investigation (equal). **Wan-Gil Jung:** Data curation (lead); Formal analysis (lead); Investigation (equal). **Jun-Seok Ha:** Resources (lead); Supervision (equal). **Ji Hoon Shim:** Resources (lead); Supervision (equal). **Jae-Hoon Park:** Resources (lead); Supervision (equal). **Sang-Wan Ryu:** Resources (lead); Supervision (equal). **Bong-Joong Kim:** Conceptualization (lead); Funding acquisition (lead); Investigation (lead); Methodology (lead); Project administration (lead); Resources (lead); Supervision (lead); Writing—original draft (lead); Writing—review & editing (lead).

Data Availability Statement

The data that support the findings of this study are available from the corresponding author upon reasonable request.

Keywords

amorphous, exsolutions, Fe_3O_4 , photoelectrochemical water-splitting, Schottky junctions

Received: August 22, 2024

Revised: October 4, 2024

Published online:

- [1] G. Chen, T. Wang, P. Liu, Z. Liao, H. Zhong, G. Wang, P. Zhang, M. Yu, E. Zschech, M. Chen, J. Zhang, X. Feng, *Energy Environ. Sci.* **2020**, *13*, 2849.
- [2] N. S. Lewis, D. G. Nocera, *Proc. Natl. Acad. Sci. U. S. A.* **2006**, *103*, 15729.
- [3] J. Suntivich, K. J. May, H. A. Gasteiger, J. B. Goodenough, Y. Shao-Horn, *Science* **2011**, *334*, 1383.
- [4] M. Kim, J. Park, M. Kang, J. Y. Kim, S. W. Lee, *ACS Cent. Sci.* **2020**, *6*, 880.
- [5] M. S. Faber, S. Jin, *Energy Environ. Sci.* **2014**, *7*, 3519.
- [6] Y. Yan, B. Y. Xia, B. Zhao, X. Wang, *J. Mater. Chem. A* **2016**, *4*, 17587.
- [7] X.-T. Xu, L. Pan, X. Zhang, L. Wang, J.-J. Zou, *Adv. Sci.* **2019**, *6*, 1801505.
- [8] D. Wang, G. Cao, in *Nanomaterials for Energy Conversion and Storage*, World Scientific Publishing Europe Ltd., London **2018**.
- [9] M. G. Walter, E. L. Warren, J. R. McKone, S. W. Boettcher, Q. M. Elizabeth, A. Santori, N. S. Lewis, *Chem. Rev.* **2010**, *110*, 6446.
- [10] C. Ding, J. Shi, Z. Wang, C. Li, *ACS Catal.* **2017**, *7*, 675.
- [11] L. Wang, Y. Zhang, W. Li, L. Wang, *Mater. Rep.: Energy* **2023**, *3*, 100232.
- [12] J. He, P. Liu, R. Ran, W. Wang, W. Zhou, Z. Shao, *J. Mater. Chem. A* **2022**, *10*, 6835.
- [13] J. Yu, Y. Dai, Q. He, D. Zhao, Z. Shao, M. Ni, *Mater. Rep.: Energy* **2021**, *1*, 100024.
- [14] Y.-F. Sun, Y.-Q. Zhang, J. Chen, J.-H. Li, Y.-T. Zhu, Y.-M. Zeng, B. S. Amirkhiz, J. Li, B. Hua, J.-L. Juo, *Nano Lett.* **2016**, *16*, 5303.
- [15] D. Neagu, G. Tsekouras, D. N. Miller, H. Ménard, J. T. S. Irvine, *Nat. Chem.* **2013**, *5*, 916.
- [16] S. Yu, D. Yoon, Y. Lee, H. Yoon, H. Han, N. Kimi, C.-J. Kim, K. Ihm, T.-S. Oh, J. Son, *Nano Lett.* **2020**, *20*, 3538.
- [17] H. Lv, L. Lin, X. Zhang, Y. Song, H. Matsumoto, C. Zeng, N. Ta, W. Liu, D. Gao, G. Wang, X. Bao, *Adv. Mater.* **2020**, *32*, 1906193.
- [18] D. Neagu, V. Kyriakou, I.-L. Roiban, M. Aouine, C. Tang, A. Caravaca, K. Kousi, I. Schreur-Piet, I. S. Metcalfe, P. Vernoux, M. C. M. van de Sanden, M. N. Tsampas, *ACS Nano* **2019**, *13*, 12996.
- [19] C. Tang, K. Kousi, D. Neagu, J. Portolés, E. I. Papaioannou, I. S. Metcalfe, *Nanoscale* **2019**, *11*, 16935.
- [20] J.-H. Myung, D. Neagu, D. N. Miller, J. T. S. Irvine, *Nature* **2016**, *537*, 528.
- [21] J. T. S. Irvine, D. Neagu, M. C. Verbraeken, C. Chatzichristodoulou, C. Graves, M. B. Mogensen, *Nat. Energy* **2016**, *1*, 15014.
- [22] O. Kwon, S. Sengodan, K. Kim, G. Kim, H. Y. Jeong, J. Shin, Y.-W. Ju, J. W. Han, G. Kim, *Nat. Commun.* **2017**, *8*, 15967.
- [23] Y. Zhu, J. Dai, W. Zhou, Y. Zhong, H. Wang, Z. Shao, *J. Mater. Chem. A* **2018**, *6*, 13582.
- [24] H. Lv, L. Lin, X. Zhang, D. Gao, Y. Song, Y. Zhou, Q. Liu, G. Wang, X. Bao, *J. Mater. Chem. A* **2019**, *7*, 11967.
- [25] D.-E. Lee, V. Devthade, S. Moru, W.-K. Jo, S. Tonda, *J. Alloys Compd.* **2022**, *902*, 163612.
- [26] X. Jia, J. Wu, K. Lu, Y. Li, X. Qiao, J. Kaelin, S. Lu, Y. Cheng, X. Wu, W. Qin, *J. Mater. Chem. A* **2019**, *7*, 14302.
- [27] Y. Zhan, C. Xu, M. Lu, Z. Liu, J. Y. Lee, *J. Mater. Chem. A* **2014**, *2*, 16217.
- [28] J. Ji, Y. Huang, J. Yin, X. Zhao, X. Cheng, S. He, X. Li, J. He, J. Liu, *ACS Appl. Nano Mater.* **2018**, *1*, 3935.
- [29] Y. Zhu, Y. Liu, Q. Ai, G. Gao, L. Yuan, Q. Fang, X. Tian, X. Zhang, E. Egar, P. M. Ajayan, J. Lou, *ACS Mater. Lett.* **2022**, *4*, 464.
- [30] X. Li, Z. Le, X. Chen, Z. Li, W. Wang, X. Liu, A. Wu, P. Xu, D. Zhang, *Appl. Catal. B* **2018**, *236*, 501.
- [31] R. Thalinger, M. Gocyla, M. Heggen, B. Klötzer, S. Penner, *J. Phys. Chem. C* **2015**, *119*, 22050.
- [32] J. Li, B. Wei, Z. Cao, X. Yue, Y. Zhang, Z. Lü, *ChemSusChem* **2018**, *11*, 254.
- [33] T. Zhu, H. E. Troiani, L. V. Moggi, M. Han, S. A. Barnett, *Joule* **2018**, *2*, 478.
- [34] K. Kim, B. Koo, Y.-R. Jo, S. Lee, J. K. Kim, B.-J. Kim, W. C. Jung, J. W. Han, *Energy Environ. Sci.* **2020**, *13*, 3404.
- [35] M.-J. Kim, M. A. Hassan, C. Lee, W.-G. Jung, H. Bae, S. H. Jeon, W. C. Jung, J.-S. Ha, J. H. Shim, J.-H. Park, S.-W. Ryu, B.-J. Kim, *Small* **2024**, *20*, 2308934.
- [36] H. Chen, C. Lim, M. Zhou, Z. He, X. Sun, X. Li, Y. Ye, T. Tan, H. Zhang, C. Yang, J. W. Han, Y. Chen, *Adv. Sci.* **2021**, *8*, 2102713.
- [37] D. A. Porter, K. E. Easterling, M. Y. Sherif, in *Phase Transformations in Metals and Alloys*, 3rd ed, CRC Press, Boca Raton **2009**.
- [38] B. S. Bokstein, B. B. Straumal, in *Diffusion in Amorphous Materials*, Springer International Publishing, Cham **2018**.
- [39] S. Liu, H. Luo, Y. Li, Q. Liu, J.-L. Luo, *Nano Energy* **2017**, *40*, 115.
- [40] Y. Zhu, L. Zhang, B. Zhao, H. Chen, X. Liu, R. Zhao, X. Wang, J. Liu, Y. Chen, M. Liu, *Adv. Funct. Mater.* **2019**, *29*, 1901783.

- [41] D. Ehre, H. Cohen, V. Lyahovitskaya, I. Lubomirsky, *Phys. Rev. B* **2008**, 77, 184106.
- [42] Q. An, F. Lv, Q. Liu, C. Han, K. Zhao, J. Sheng, Q. Wei, M. Yan, L. Mai, *Nano Lett.* **2014**, 14, 6250.
- [43] A. G. Nene, M. Takahashi, P. R. Somani, *World J. Nano Sci. Eng.* **2016**, 6, 20.
- [44] Q. Ai, Z. Yuan, R. Huang, C. Yang, G. Jiang, J. Xiong, Z. Huang, S. Yuan, *J. Mater. Sci.* **2019**, 54, 4212.
- [45] A. Kumar, A. Rana, G. Sharma, M. Naushad, A. H. Al-Muhtaseb, C. Guo, A. Iglesias-Juez, F. J. Stadler, *ACS Appl. Mater. Interfaces* **2018**, 10, 40474.
- [46] S. Kawasaki, R. Takahashi, T. Yamamoto, M. Kobayashi, H. Kumigashira, J. Yoshinobu, F. Komori, A. Kudo, M. Lippmaa, *Nat. Commun.* **2016**, 7, 11818.
- [47] A. Abdullah, I. V. Bagal, A. Waseem, M. A. Kulkarni, H. Thaalbi, J. K. Lee, S.-W. Ryu, *Mater. Today Phys.* **2022**, 28, 100846.
- [48] T.-F. Hou, A. Shanmugasundaram, M. A. Hassan, M. A. Johar, S.-W. Ryu, D.-W. Lee, *Int. J. Hydrogen Energy* **2019**, 44, 19177.
- [49] Z. Lin, C. Du, B. Yan, G. Yang, *J. Catal.* **2019**, 372, 299.
- [50] K. Xu, M. Yao, J. Chen, P. Zou, Y. Peng, F. Li, X. Yao, *J. Alloys Compd.* **2015**, 653, 7.
- [51] Y. Chen, L. Wang, W. Wang, M. Cao, *Appl. Catal. B* **2017**, 209, 110.
- [52] M. Ebaid, D. Priante, G. Liu, C. Zhao, M. S. Alias, U. Buttner, T. K. Ng, T. T. Isimjan, H. Idriss, B. S. Ooi, *Nano Energy* **2017**, 37, 158.
- [53] G. L. He, Y.-H. Zhong, M.-J. Chen, X. Li, Y.-P. Fang, Y.-H. Xu, *J. Mol. Catal. A: Chem.* **2016**, 423, 70.
- [54] Y. Liu, X. Xu, S. Lv, H. Li, Z. Si, X. Wu, R. Ran, D. Weng, *Catal. Sci. Technol.* **2021**, 11, 3039.
- [55] A. Aguinaco, J. M. Manuel, E. Blanco, M. Domínguez, R. Litrán, J. J. Delgado, M. Ramírez-del-Solar, *Materials* **2022**, 15, 6718.
- [56] A. S. Reddy, J. Kim, *Appl. Surf. Sci.* **2020**, 513, 145836.
- [57] J. Resasco, H. Zhang, N. Kornienko, N. Becknell, H. Lee, J. Guo, A. L. Briseno, P. Yang, *ACS Cent. Sci.* **2016**, 2, 80.
- [58] Z. Zhong, W. Cheng, X. Chen, J. Li, H. Yang, L. Zhang, P. Yang, *J. Mater. Sci: Mater. Electron.* **2024**, 35, 244.
- [59] A. Hankin, F. E. Bedoya-Lora, J. C. Alexander, A. Regoutz, G. H. Kelsall, *J. Mater. Chem. A* **2019**, 7, 26162.
- [60] C. Liu, H. Luo, Y. Xu, W. Wang, Q. Liang, N. Mitzusaki, Z. Chen, *J. Mater. Sci.* **2019**, 54, 10670.
- [61] L. Zhang, Z. Dai, G. Zheng, Z. Yao, J. Mu, *RSC Adv.* **2018**, 8, 10654.
- [62] Y. Miao, J. Liu, L. Chen, H. Sun, R. Zhang, J. Guo, M. Shao, *Chem. Eng. J.* **2022**, 427, 131011.
- [63] S. Dadgostar, J. L. P. Ruiz, J. S. Gutierrez, B. Lepine, P. Schieffer, J. Jimenez, *Mater. Sci. Eng. B* **2022**, 283, 115830.
- [64] S. Bera, S. A. Lee, W.-J. Lee, M. Ilka, J.-H. Kim, C.-M. Kim, H. Khan, H. W. Jang, S.-H. Kwon, *ACS Appl. Mater. Interfaces* **2020**, 12, 48486.
- [65] V. L. Deringer, A. L. Tchougréeff, R. Dronskowski, *J. Phys. Chem. A* **2011**, 115, 5461.
- [66] S. F. Matar, A. Villesuzanne, M. Uhl, *J. Mater. Chem.* **1996**, 6, 1785.
- [67] X. Li, H. Wang, Z. Cui, Y. Li, S. Xin, J. Zhou, Y. Long, C. Jin, J. B. Goodenough, *Sci. Adv.* **2019**, 5, 6262.
- [68] C. Zhang, C.-L. Wang, J.-C. Li, K. Yang, *Chin. Phys.* **2007**, 16, 1422.
- [69] K. van Benthem, C. Elsässer, M. Rühle, *Phys. Rev. B* **2005**, 72, 125435.
- [70] K. van Benthem, C. Elsässer, R. H. French, *J. Appl. Phys.* **2001**, 90, 6156.
- [71] T. Ochs, S. Köstlmeier, C. Elsässer, *Integr. Ferroelectr.* **2001**, 32, 267.
- [72] A. López-García, L. Almar, S. Escolástico, A. B. Hungria, A. J. Carrillo, J. M. Serra, *ACS Appl. Energy Mater.* **2022**, 5, 13269.
- [73] P. Błaszczak, M. Łapinski, S.-F. Wang, P. Jasinski, B. Bochentyn, *Int. J. Hydrogen Energy* **2020**, 45, 29186.
- [74] B. Rudolph, A. I. Tsiotsias, B. Ehrhardt, P. Dolcet, S. Gross, S. Haas, N. D. Charisou, M. A. Goula, S. Mascotto, *Adv. Sci.* **2023**, 10, 2205890.
- [75] X. Cao, L. Ke, K. Zhao, X. Yan, X. Wu, N. Yan, *Chem. Mater.* **2022**, 34, 10484.
- [76] N. Yu, G. Jiang, T. Liu, X. Chen, M. Miao, Y. Zhang, Y. Wang, *Sustainable Energy Fuels* **2021**, 5, 401.
- [77] L. Tang, Z. Chen, F. Zuo, B. Hua, H. Zhou, M. Li, J. Li, Y. Sun, *Chem. Eng. J.* **2020**, 401, 126082.
- [78] M. Kim, J. Park, H. Ju, J. Y. Kim, H.-S. Cho, C.-H. Kim, B.-H. Kim, S. W. Lee, *Energy Environ. Sci.* **2021**, 14, 3053.
- [79] K. G. Both, V. M. Reinertsen, T. M. Aarholt, I. J. T. Jensen, D. Neagu, Ø. Prytz, T. Norby, A. Chatzidakis, *Catal. Today* **2023**, 413–415, 113950.